A LTE-Based Channel Measurement Method for High-Speed Railway Communications

Tao Zhou[1], Cheng Tao[1], Sana Salous[2], Liu Liu[1], Zhenhui Tan[1]

[1]Institute of Broadband Wireless Mobile Communications, Beijing Jiaotong University, Beijing 100044, P.R.China

[2]School of Engineering and Computing Sciences, Durham University, Durham DH1 3LE, UK

Email: taozhou.china@gmail.com, chtao@bjtu.edu.cn, sana.salous@durham.ac.uk, {liuliu, zhhtan}@bjtu.edu.cn

Abstract

Because of the measurement restriction and measurement efficiency issues of applying conventional channel sounders in high-speed railway (HSR) scenarios, railway network based channel measurement methods have recently attracted much attention. A method that employs long-term evolution (LTE) railway networks to achieve channel measurements for HSR communications is presented. The principle of the method is described and the channel sounding performance is analyzed. The method is implemented by a novel measurement system which can enable the collection of time-frequency-space channel data. Based on the system, field measurements that consider both direct and relay coverage schemes are conducted on Beijing to Tianjin HSR in China. Measurement data are partitioned into single-link case in which the common channel parameters can be extracted and multi-link case in which the correlation between different links can be characterized. Finally, statistical results, involving path loss (PL), Ricean K-factor, root mean square (RMS) delay spread (DS), single-link spatial correlation (SC) and multi-link SC, are presented, which not only confirm the viability of the proposed method but also provide realistic channel characteristics available for the study of both existing HSR LTE systems and future HSR dedicated systems.

Index Terms

Channel measurement, high-speed railway, long-term evolution (LTE), propagation characterization, multi-link spatial correlation

I. Introduction

High speed railway (HSR) communications, consisting of professional communication and public

communication, are essential parts in the whole HSR system. The professional communication aims at guaranteeing the security of railway operation, whereas the public communication is to meet the in-journey experience of passengers. The leading global system for mobile communications for railway (GSM-R) is primarily in charge of the train control data transmission, which can only provide low data rate services, e. g., dispatching, shunting, and maintenance. Professional broadband services, involving onboard video surveillance and track monitoring, as well as public services, such as Internet access, online TV, and mobile services, far exceed the capability of GSM-R. In fact, the next-generation HSR dedicated communication system is envisioned to achieve professional and public broadband communications simultaneously [1].

Since the radio channel determines the performance of wireless communication systems, detailed knowledge and accurate characterization of its parameters in realistic HSR propagation scenarios is crucial. The majority of radio channel models used for system simulation are based on extensive channel measurement data. Therefore, channel measurements are the precondition for the design of HSR communication systems and the evaluation of HSR communication technologies.

Though measurement campaigns on HSR are expensive, time-consuming, and difficult to carry out, a few HSR channel measurements have been conducted, which can be classified into two categories:

1) ***Channel sounder based measurements.*** There are only several measurement campaigns [2-4] taken under high mobility conditions using commercial channel sounders, such as RUSK and Propsound. And non-commercial channel sounders [5-6] have not yet been used in the HSR channel measurements until now. One of the first reported HSR measurements employed the RUSK sounder to measure the single-input multiple-output (SIMO) relay channel in Germany [2]. Propsound HSR channel measurements in rural and hilly scenarios in Taiwan were reported in [3]. The direct link was considered to measure the SIMO and the multiple-input single-output (MISO) channel. Further, single-input single-output (SISO) mobile relay channel measurements using Propsound were carried out in viaduct scenarios on HSR in China [4]. However, there are still no reported multiple-input multiple-output (MIMO) channel measurements in a specific HSR scenario utilizing the standard channel sounders.
2) ***Railway network based measurements.*** Due to the measurement restriction and measurement efficiency issues of applying traditional channel sounders in HSR scenarios [7], since 2011 some researchers resorted to railway network based channel measurement methods. A series of GSM-R channel measurements were conducted in viaduct scenarios on HSR in China [8]. For channel

characterization purposes, the GSM-R signal is regarded as a narrowband continuous waveform (CW) signal and hence not suitable for wideband measurements. To enable the wideband channel characterization, the common pilot channel (CPICH) signal in WCDMA railway networks was collected and analyzed to extract the multipath properties [9]. Unfortunately, the measurement bandwidth of this method does not meet the requirements of the future HSR dedicated communication system, and it lacks the spatial sounding ability.

To the best of our knowledge, existing HSR channel measurement data are insufficient for the design of the next-generation HSR dedicated communication system. It is necessary to carry out more measurements for the further HSR channel characterization. Reported measurement campaigns do not provide a suitable approach with the potential of enabling comprehensive and efficient HSR channel measurements. In recent years, there have been large-scale deployments of long term evolution (LTE) networks around the world. In particular, the LTE railway networks have almost covered all HSRs in China, for a total of 15,000 km by 2014, and as HSRs continue to grow, the LTE railway networks that grow with them will exceed 30,000 km in 2020 [10]. Depending on the current LTE railway networks, we present and implement a LTE-based HSR channel measurement method. The contributions and novelties of this paper are summarized as follows:

1) A channel sounding method that employs the cell-specific reference signal (CRS) of LTE as the excitation signal is proposed to extract the channel impulse response (CIR). The CIR performance is analyzed by considering impacts of carrier frequency offset (CFO) and timing offset (TO).
2) A channel measurement system composed of the LTE railway network and the LTE sounder is built up for the collection of time-frequency-space channel data. SISO and MIMO channel measurements considering direct coverage (DC) and relay coverage (RC) schemes are conducted on Beijing to Tianjin (BT) HSR in China. The measurement data are further partitioned into single-link case and multi-link case, which enable not only single-link channel characterization but also multi-link channel characterization.
3) Based on the measurement data, in addition to the conventional HSR channel characteristics, e. g., path loss (PL), Ricean K-factor, and root mean square (RMS) delay spread (DS), spatial correlations (SCs), involving single-link and multi-link SCs, are derived and analyzed. These results confirm the viability of the proposed method and provide the useful information for the optimization of the current HSR LTE system and the design of the next-generation HSR dedicated communication system.

The remainder of this paper is outlined as follows. Section II presents the LTE-based channel sounding method. In Section III, the LTE-based HSR channel measurement campaigns are described. Measurement results are derived and analyzed in Section IV. Finally, conclusions are drawn in Section V.

II. LTE-Based Channel Sounding Method

In this section, the frame structure of the excitation signal will be described firstly. Then the principle and methodology for CIR extraction will be presented. After that, impacts of CFO and TO on the CIR performance will be analyzed.

A. Excitation Signal

LTE supporting frequency division duplexing (FDD) and time division duplexing (TDD) adopts orthogonal frequency division multiplexing (OFDM) and MIMO technologies. Typical deployed carrier frequencies are in the range of 400 MHz to 4 GHz, with scalable carrier bandwidths from 1.4 MHz to 20 MHz. The time-frequency-space FDD LTE frame structure is shown in Fig. 1. One radio frame of 10 ms is subdivided into ten 1 ms subframes, each of which is split into two 0.5 ms slots. In the case of the normal cyclic prefix (CP), one slot comprises seven OFDM symbols and the spacing of subcarriers in one OFDM symbol is 15 kHz. The CRS embedded in the time-frequency-space plane is used for channel estimation in the LTE downlink. When it comes to channel sounding, the CRS can be regarded as a kind of excitation waveform, whose signal structure determines the measurement capability. As shown in Fig. 1, in the time direction, the maximum repetition period of the CRS is 0.5 ms, corresponding to 2 kHz channel sampling rate and 1 kHz maximum expected Doppler shift. In the frequency direction, there is one reference symbol of the CRS every six subcarriers with a spacing of 90 kHz on each OFDM symbol. This spacing determines the maximum time delay window of 11 μs. In the case of 20 MHz LTE, the total number of reference symbols on each OFDM symbol is 200, which corresponds to 18 MHz measurement bandwidth and 56 ns time delay resolution. In the space direction, when a resource element (RE) carries the reference symbol on one antenna port, the corresponding RE on another antenna port is unused. This guarantees the orthogonality of the CRSs on the 4 antenna ports, thus enabling the MIMO channel measurement with the full parallel architecture [11] at the transmitter.

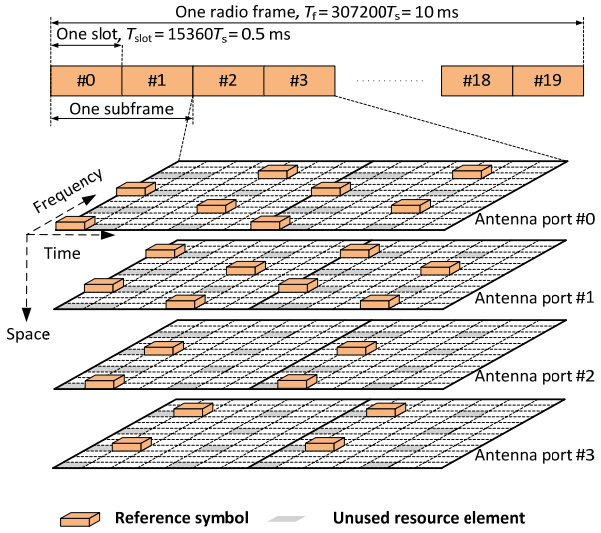

Fig. 1 The time-frequency-space FDD LTE frame structure

Denoting the complex-valued LTE signal on the i-th subcarrier of one OFDM symbol as $S(i)$, the transmitted signal in radio frequency (RF) is given by

$$x(t) = \frac{1}{N}\sum_{i=0}^{N-1} S(i) e^{j2\pi it/T_s + j(2\pi f_c t + \phi)}, i = 0,1,\ldots,N-1 \qquad (1)$$

where N is the number of subcarriers on one OFDM symbol, T_s denotes the sampling period, f_c indicates the center frequency, and ϕ represents the carrier phase. The embedded CRS is quadrature phase shift keying (QPSK) modulated, which can be written as [12]

$$S(k) = \frac{1}{\sqrt{2}}\left(1-2\cdot c(2k)\right) + j\frac{1}{\sqrt{2}}\left(1-2\cdot c(2k+1)\right), k = 0,1,...,M-1, \qquad (2)$$

where M is the number of CRSs on one OFDM symbol and $c(x)$ is a length-31 Gold sequence with different initialization values depending on the cell identity (ID). The CRS is similar to the multi-carrier spread spectrum signal (MCSSS) applied in the RUSK sounder, which not only ensures precise concentration of the energy in the band of interest but also enables correlation gain based on the frequency domain correlation processing [13]. The correlation gain of the CRS is $10\log M$, e.g., in the case of 20 MHz LTE, $M = 200$ and the correlation gain is about 23 dB. In Fig. 2, an example of the CRS during one frame period in the case of 20 MHz LTE is given in time and frequency domains.

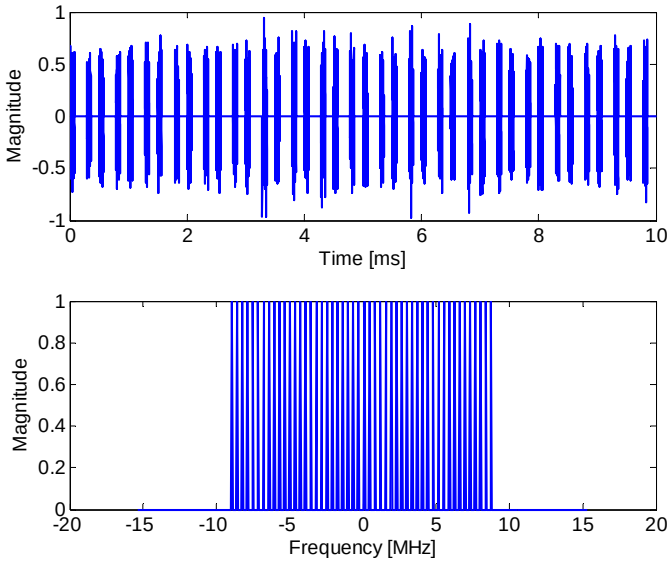

Fig. 2 CRS waveform in time and frequency domains

B. CIR Extraction

The transmitted excitation signal will experience the propagation fading in time, frequency and space. Denoting the time-variant multipath channel between one transmitter and one receiver as $h(t,k)$, the received signal is the convolution of the transmitted signal and the channel, expressed as

$$y(t) = x(t) * h(t,k) + \eta(t), \tag{3}$$

where $*$ represents the convolution operation and $\eta(t)$ is the additive white Gaussian noise (AWGN).

At the receiver, the discrete-time baseband signal can be acquired according to down conversion and A/D sampling, written as

$$\begin{aligned} r(n) &= y(t)\big|_{t=nT_s-\Delta t}\, e^{-j\left(2\pi \hat{f}_c t+\hat{\phi}\right)} \\ &= \left[\frac{1}{N}\sum_{i=0}^{N-1} S(i) e^{j2\pi i(nT_s-\Delta t)/(NT_s)} e^{-j\left[2\pi\Delta f_c(nT_s-\Delta t)\right]}\right] * h(n,k) + \eta'(n), \end{aligned} \tag{4}$$

where $\Delta f_c = \hat{f}_c - f_c$ indicates the CFO, Δt denotes the TO, and $\eta'(n) = \eta(n) e^{-j\left(2\pi \hat{f}_c nT_s+\hat{\phi}\right)}$.

Here, we take one OFDM symbol as an example to explain the CIR extraction. Assume that frame and slot synchronizations are achieved. After the discrete Fourier transform (DFT) operation, the received signal in the frequency domain can be represented as

$$
\begin{aligned}
R(i) &= \sum_{n=0}^{N-1} r(n) e^{-j2\pi ni/N} \\
&= \frac{1}{N}\sum_{m=0}^{N-1} H(k) S(m) \sum_{n=0}^{N-1} e^{j2\pi n\left[(m-i)/N - \Delta f_c T_s\right]} e^{-j2\pi m\Delta t/(NT_s) + j2\pi \Delta f_c \Delta t} + \eta''(i) \\
&= \frac{1}{N}\sum_{m=0}^{N-1} H(k) S(m) \frac{1-e^{j2\pi\left[(m-i)-N\Delta f_c T_s\right]}}{1-e^{j2\pi\left[(m-i)/N - \Delta f_c T_s\right]}} e^{-j2\pi m\Delta t/(NT_s) + j2\pi \Delta f_c \Delta t} + \eta''(i),
\end{aligned}
\tag{5}
$$

where $\eta''(i) = \eta'(i) e^{-j2\pi i/N}$.

The CRS, $R(k)$, can be extracted from the received frequency domain signal according to the CRS pattern in the LTE frame structure. Then, the frequency domain correlation processing is performed as

$$
\begin{aligned}
\hat{H}(k) &= R(k) S^*(k) \\
&= \frac{1}{M}\sum_{m=0}^{M-1} H(k) S(m) S^*(k) \frac{1-e^{j2\pi\left[(m-k)-M\Delta f_c T_s\right]}}{1-e^{j2\pi\left[(m-k)/M - \Delta f_c T_s\right]}} e^{-j2\pi m\Delta t/(MT_s) + j2\pi \Delta f_c \Delta t} \\
&\quad + \eta''(k) S(m) S^*(k),
\end{aligned}
\tag{6}
$$

where $(\cdot)^*$ denotes the conjugation operation.

Finally, the estimation of the CIR can be obtained from (6) via the inverse DFT (IDFT) as

$$
\begin{aligned}
\hat{h}(z) &= \frac{1}{M}\sum_{k=0}^{M-1} \hat{H}(k) e^{j2\pi kz/M} \\
&= \frac{1}{M^2}\sum_{k=0}^{M-1} H(k) \frac{1-e^{-j2\pi \Delta f_c MT_s}}{1-e^{-j2\pi \Delta f_c T_s}} e^{-j2\pi k\Delta t/(MT_s) + j2\pi \Delta f_c \Delta t + j2\pi kz/M} \\
&\quad + \frac{1}{M^2}\sum_{k=0}^{M-1}\sum_{m=0, m\neq k}^{M-1} H(k) S(m) S^*(k) \frac{1-e^{j2\pi\left[(m-k)-M\Delta f_c T_s\right]}}{1-e^{j2\pi\left[(m-k)/M - \Delta f_c T_s\right]}} \\
&\quad \cdot e^{-j2\pi m\Delta t/(MT_s) + j2\pi \Delta f_c \Delta t + j2\pi kz/M} + \eta'''(k),
\end{aligned}
\tag{7}
$$

where $z = 0, 1, \ldots, M-1$ and $\eta'''(k) = \frac{1}{M}\sum_{k=0}^{M-1} \eta''(k) S(m) S^*(k) e^{j2\pi kz/M}$. In (7), the first term refers to the expected CIR with the impacts of CFO and the TO, the second term stands for the inter-carrier interference (ICI) effect, and the third term is the AWGN.

C. CIR Performance Analysis

Impact of CFO on CIR: In order to analyze the independent impact of CFO on the extracted CIR, setting $\Delta t = 0$ and $\eta'''(k) = 0$. Thus, the equation (7) is written as

$$\hat{h}(z) = h(z)\left(\frac{1}{M}\frac{1-e^{-j2\pi M\Delta f_c T_s}}{1-e^{-j2\pi\Delta f_c T_s}}\right) + \frac{1}{M^2}\sum_{k=0}^{M-1}\sum_{m=0,m\neq k}^{M-1} H(k)S(m)S^*(k)\frac{1-e^{j2\pi\left[(m-k)-M\Delta f_c T_s\right]}}{1-e^{j2\pi\left[(m-k)/M-\Delta f_c T_s\right]}}e^{j2\pi kz/M}. \quad (8)$$

The normalized CIR can be expressed by

$$\hat{h}_n(z) = h(z) + \frac{1}{M}\sum_{k=0}^{M-1}\sum_{m=0,m\neq k}^{M-1} H(k)S(m)S^*(k)\frac{1-e^{-j2\pi\Delta f_c T_s}}{1-e^{j2\pi\left[(m-k)/M-\Delta f_c T_s\right]}}e^{j2\pi kz/M} = h(z) + I(z,\Delta f_c), \quad (9)$$

where $I(z,\Delta f_c)$ represents the ICI effect with different CFOs. Equation (9) means that the CFO causes an additive interference on the normalized CIR, in other words, the CFO has an influence on the noise floor in the CIR measurement. Fig. 3 illustrates the simulation result of magnitude square of the normalized CIR in the case of different CFOs using the 20 MHz LTE signal. It can be seen that the CFO raises the noise floor and decreases the dynamic range of multipath identification. In addition, the CFO yields an extra frequency shift, which will affect the measurement of Doppler characteristics. In practice, to avoid the CFO in the outdoor channel measurement, a common way is the use of Rubidium or GPS reference clock, which can guarantee the frequency consistency at the transceiver.

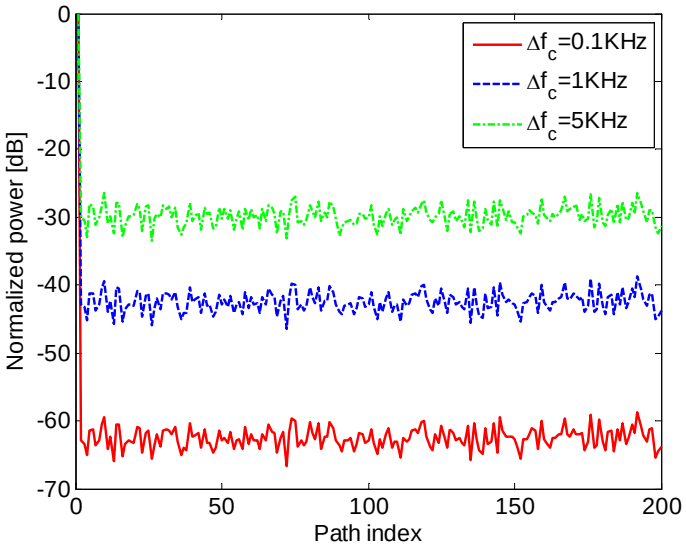

Fig. 3 Magnitude square of the normalized CIR in the case of different CFOs using the 20 MHz LTE signal.

Impact of TO on CIR: Setting $\Delta f_c = 0$ and $\eta'''(k) = 0$, the isolated impact of TO on the extracted CIR is highlighted. Equation (7) is simplified as

$$\begin{aligned}\hat{h}(z) &= \sum_{k=0}^{M-1} H(k)\left(\frac{1}{M}e^{-j2\pi k\Delta t/MT_s}\right)e^{j2\pi kz/M} \\ &= \frac{1}{M}\sum_{k=0}^{M-1} H(k)e^{j2\pi k(z-\Delta t/T_s)/M} \\ &= h(z-\Delta t/T_s),\end{aligned} \tag{10}$$

where $\Delta t = \Delta t_1 + \Delta t_2$. Δt_1 and Δt_2 denote the integer TO and fractional TO, respectively. The integer TO leads to the cyclic shift of the CIR, which has no influence on the power and relative delay estimation of the multipath, whereas the fractional TO causes the power leakage of the CIR. Fig. 4 shows the simulation result of magnitude square of the normalized CIR in the case of different fractional TOs using the 20 MHz LTE signal. It is observed that the leakage severity of the CIR is more serious with the increase of the fractional TO, and maximum leakage appears at $\Delta t_2 = 0.5T_s$. The leaked power exponentially spreads to other paths, which will affect the power estimation of the multipath. In [14], a hanning window function with a narrow mainlobe and low sidelobes is applied to reduce the power leakage of the CIR. In this paper, we use the simple windowing method to tackle the fractional TO issue.

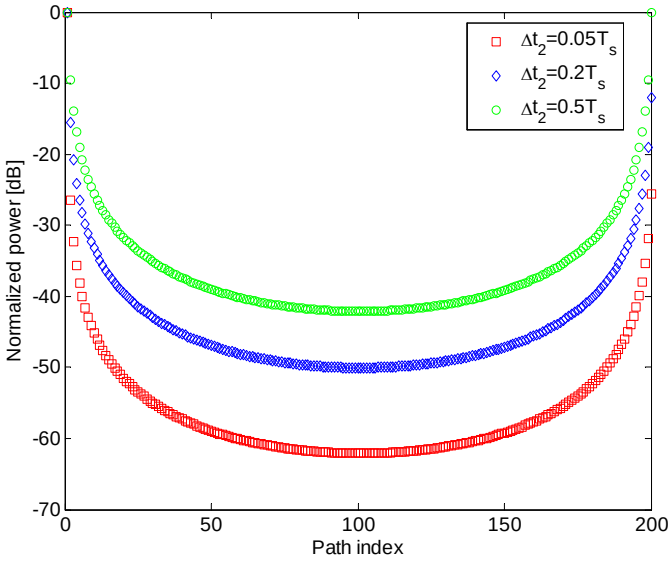

Fig. 4 Magnitude square of the normalized CIR in the case of different fractional TOs using the 20 MHz LTE signal.

III. LTE-Based HSR Channel Measurement Campaigns

This section will report on the implementation of LTE-based HSR channel measurement campaigns. We will first show the setup of the measurement system, and subsequently will describe the field measurements. We will also make a classification for the measurement data.

A. Measurement System Setup

The setup of the LTE-based HSR channel measurement system is shown in Fig. 5. This system consists of the LTE railway network and the LTE sounder. The LTE sounder is used to collect the time-frequency-space channel data in the whole railway line, which makes continuous measurements feasible and thus improves the measurement efficiency.

Unlike the conventional cellular network, the railway network adopts a narrow strip coverage mode and a building baseband unit (BBU) plus remote radio unit (RRU) structure. One base station (BS) site has two RRUs which employ directional antennas to transmit radio frequency (RF) signals in opposite directions along the track. Cell combination technology [10] is used in this network, which combines several RRUs into a big narrow-strip-shaped cell via optical fiber. These RRUs are controlled by the BBU that is in charge of RF signal processing. Due to such a dedicated structure, the entire network can be classified into two categories: non-overlapped coverage region and overlapped coverage region. In the non-overlapped coverage area, only one signal from one BS is received. In the overlapped area, however, the two same signals from neighboring BSs arrive at the receiver simultaneously. From the delay domain perspective, these two signals can be distinguished according to different propagation delays.

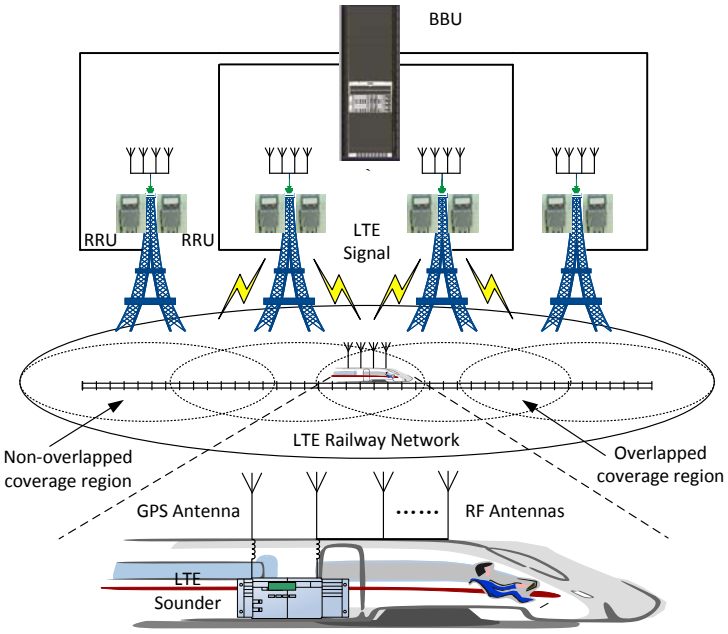

Fig. 5 LTE-based channel measurement system

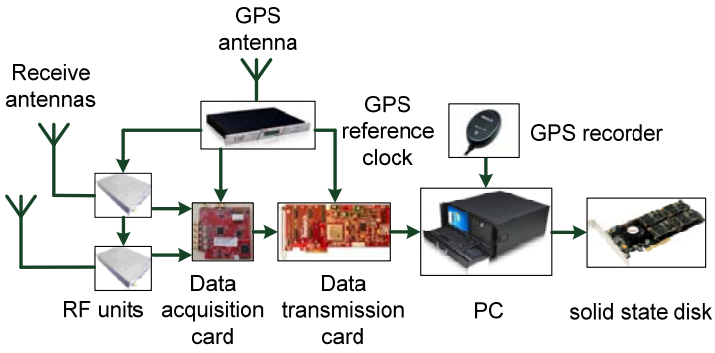

Fig. 6 Hardware diagram of LTE sounder

Different from the conventional channel sounders, the LTE sounder has only a receiver as shown in Fig. 6. The LTE sounder consists of two RF units, a data acquisition card, a data transmission card, a GPS reference clock, a PC, a solid state disk (SSD) as well as a GPS recorder. The receive antennas are connected to the RF units that output 70 MHz intermediate frequency (IF) signals. High-frequency down-converter of the RF unit uses a broad frequency synthesizer in the range of 20 MHz-3 GHz (which can be configured with a step of 100 kHz) and a bandwidth of 20 MHz [15]. Automatic gain control (AGC) of the RF unit can be disabled, and the RF gain can be controlled. The outputs of the RF units are transferred to the data acquisition card where the IF signals are sampled in a dual-channel 14-bit A/D convertor (ADC) with a maximum sampling rate of 105 MSPS. The ADC is configured operating at 56 MSPS to meet the requirement of band-pass sampling in the case of 70 MHz IF and 20 MHz bandwidth. In the data transmission card, the digitized IF signal transmission is controlled by a Virtex-5 FPGA and a DDR2 SDRAM is employed to bridge data streams between the PC memory and the ADC. The PC stores the collected data in the high-speed SSD [16] with 1TB capacity storage memory. The GPS reference clock [17] with 10^{-11} frequency accuracy provides a common 10 MHz reference clock signal for the RF units, data acquisition card and data transmission card. In addition, the GPS recorder is used to collect the real-time navigation data involving GPS, time, and speed information.

B. Field Measurement Description

Based on the established system, field measurements are performed on BT HSR in China. Fig. 7 illustrates the LTE network structure and propagation environment on BT HSR. The chosen network covers about 16 km distance with 15 BSs and 30 RRUs. The maximum spacing between neighboring BSs is around 1.2 km. There are two types of cell structures serving for 2605 MHz and 1890 MHz networks, respectively. The 2650 MHz network has 6 cells, each of which contains 3 BSs or 2 BSs, whereas the 1890 MHz network

has 3 bigger cells with 5 BSs each. The BS is generally less than 20 m away from the railway which is built on viaduct. There are three typical BS heights, such as 10 m, 20 m and 35 m, which indicate the vertical distance between the BS antenna and the viaduct. Along the railway line, plain is the main propagation environment where there are usually a large range of open area, light forestation or a few buildings with an average height of less than 10 m.

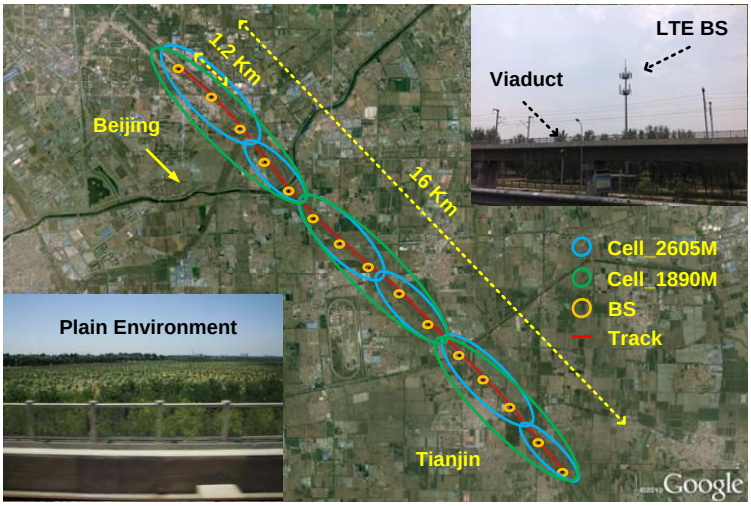

Fig. 7 LTE network structure and propagation environment on BT HSR

Two HSR wireless coverage schemes, DC and RC, are considered in our measurements. SISO channel measurements are carried out using the 2650 MHz network for the DC scenario, whereas 2×2 MIMO channel measurements are performed employing the 1890 MHz network for the RC scenario. Fig. 8 shows the measurement equipment in the two scenarios and Tab. 1 lists the corresponding measurement parameters. At the transmitter, the BS uses ±45° cross-polarized directional antennas to transmit the CRSs with the power of 12.2 dBm. At the receiver, as for the RC case, the LTE sounder adopts the professional train-mounted antennas, HUBER+SUHNER [18], to receive the excitation signal. In the test, antennas 5 and 6 with the spacing of 1.2 m (7.6 wavelengths at 1890 MHz) are chosen for the MIMO measurement, antenna 3 is connected to spectrum analyzer to monitor the signal state, and antenna 1 is used to receive the GPS signal. With regard to the DC case, a bi-conical antenna with better antenna radiation pattern is utilized and placed close to the window of the train carriage.

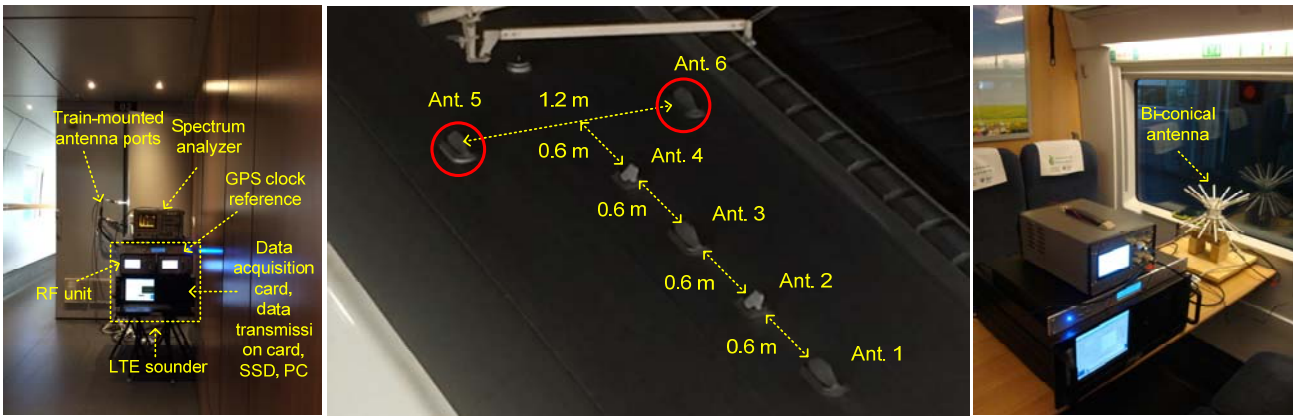

(a) (b) (c)

Fig. 8 Measurement equipment in the two scenarios. (a) RC case. (b) Structure of train-mounted antennas. Antennas 1, 3, 5, 6 can be used for the wideband signal test, while antennas 2 and 4 can only be available for the specific GSM-R network. (c) DC case.

Tab. 1 Measurement parameters

Measurement scenario	DC	RC
Measurement frequency [MHz]	2605	1890
Measurement bandwidth [MHz]	18	18
CRS Transmitted power [dBm]	12.2	12.2
Transmit antenna type	±45° cross-polarized	±45° cross-polarized
Transmit antenna gain [dBi]	18.6	17.4
Horizontal half-power beamwidth of transmit antenna [deg]	60	67
Vertical half-power beamwidth of transmit antenna [deg]	4.9	6.6
Electric tilted angle of transmit antenna [deg]	3	3
Receive antenna type	Bi-conical	HUBER+SUHNER
Receive antenna gain [dBi]	0	8.5
Receive antenna number	1	2
Receive antenna spacing [m]	-	1.2 (7.6 wavelengths)
Train velocity [km/h]	285	285

C. Measurement Data Partitioning

Since the measurement data are collected in both the non-overlapping and overlapping areas of the network, they can be reasonably partitioned into two cases: single-link and multi-link measurement data. As shown in Fig. 9, we take an example of the power delay profile (PDP) and Doppler power spectral density (DPSD) in one cell in the RC scenario to explain how to partition the measurement data. In Fig. 9(a), the time-variant PDP during the first 35 s period in the cell is plotted. Two obvious PDP transitions regarding BS1 and BS2 whose positions are identified by the white circles are highlighted. When the train enters into the non-overlapping area, we define a single-link region where the propagation link between BS1 and the train, indicated by PDP (i), occupies the whole time delay window. However, once the train moves into the

overlapping area between BS1 and BS2, another propagation link between BS2 and the train, denoted by PDP (ii), appears in the time delay window as well. We regard this area as a multi-link region where the time delay window covers two links simultaneously. In the multi-link region, the time delay window can be divided into two parts: one is for PDP (i) and another is for PDP (ii), as illustrated in Fig. 9(b). As the train is moving away from BS1, the delay difference $\Delta\tau$ between PDP (i) and PDP (ii) is gradually shortening. If the train travels at the crossing point marked with a red circle in Fig. 9(a), the PDP (i) and PDP (ii) would be indistinguishable, e. g., $\Delta\tau = 0$. Since $\Delta\tau$ determines the time delay window of PDP (i), a threshold, $\Delta\tau = 1\mu s$, is set to enable the coverage of most multipath components. Fig. 9(c) plots the corresponding time-variant DPSD result. When the train passes through the coverage of BS1 and BS2, two typical Doppler transitions from the maximum positive frequency to the minimum negative frequency are observed and marked as DPSD (i) and DPSD (ii). In the single-link region only DPSD (i) exists, while in the multi-link area DPSD (i) and DPSD (ii) appear at the same time, as shown in Fig. 9(d). The two DPSDs have the same maximum Doppler shift but opposite angles of arrival.

In the single-link region we express the measured CIR as H_{ij}^{S} and in the multi-link region we extract the CIRs from BS1 and BS2 according to the above analysis, represented as $\mathrm{H}_{ij}^{M,1}$ and $\mathrm{H}_{ij}^{M,2}$. Note that i and j are the indices of the antenna elements at the BS and the receiver sides, respectively. In addition, we choose 6 groups of DC measurement data and 3 groups of RS measurement data, each of which corresponds to one cell. Then, we average all the results derived from these measurement data to analyze the channel characteristics in the whole network.

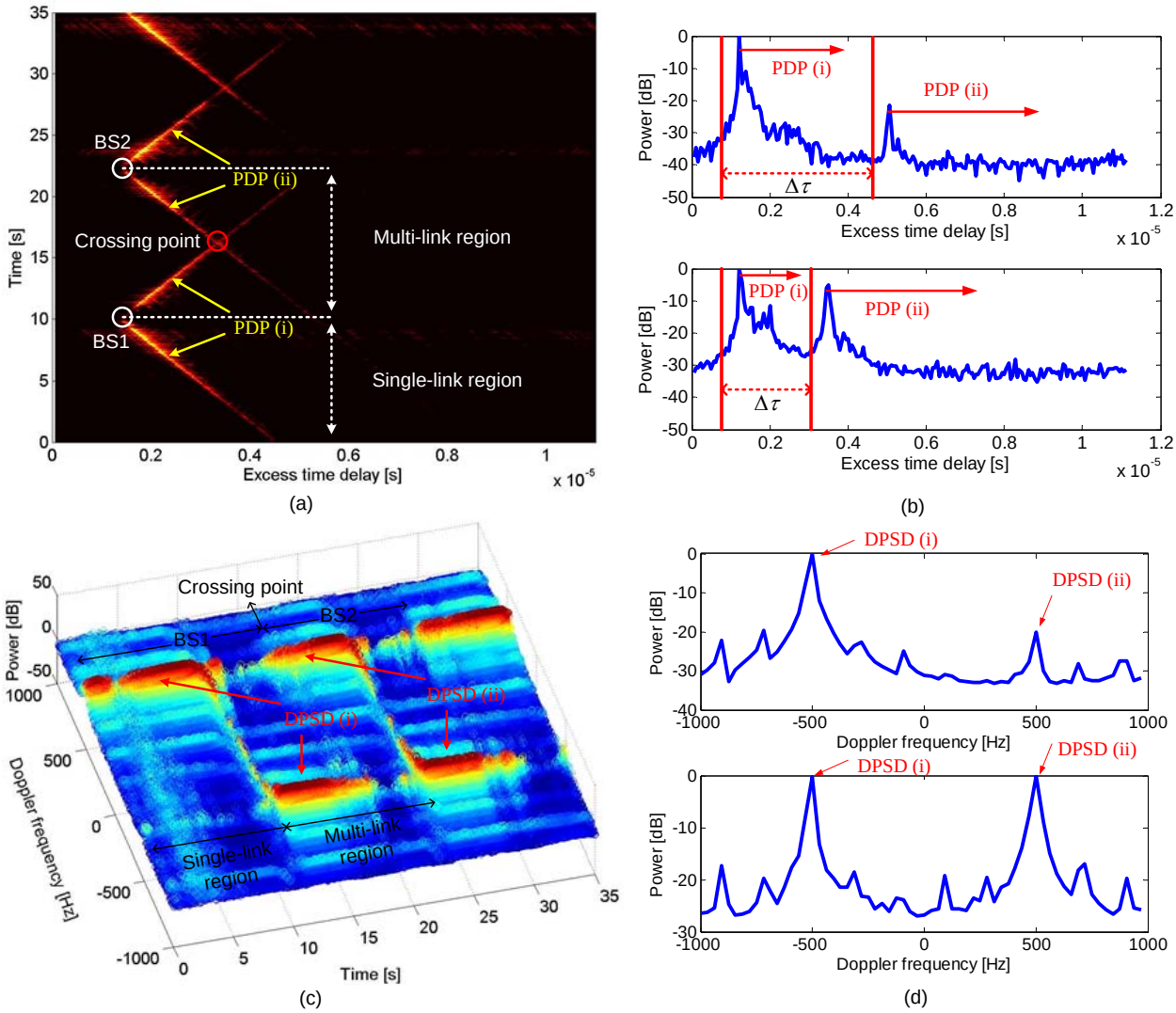

Fig. 9 An example of the measured PDP and Doppler PSD in one cell in the RC scenario. (a) Time-variant PDP. (b) Two snapshots of the PDP in the multi-link region. The top one is captured when the train is close to BS1, whereas the bottom one is recorded when the train moves away from BS1. (c) Time-variant DPSD. (d) Two snapshots of the DPSD in the multi-link region. The top one is acquired when the train goes away from BS1, whereas the bottom one is obtained when the train is close to the crossing point.

IV. Measurement Results and Analysis

In this section, we first focus on the traditional channel characteristics, involving PL, Ricean K-factor, RMS DS, and single-link SC, which are extracted using the measurement data in the single-link region. We also analyze the multi-link SC based on the measurement data in the multi-link region.

A. Path Loss

To extract the PL, the measured CIR should be averaged within a local area, where the condition of wide-sense stationary and uncorrelated scattering (WSSUS) is satisfied. The averaged length is commonly chosen to be 20 wavelengths in the mobile measurement [19]. The PL is conventionally modeled as a function of logarithmic distance. The estimated PL models in dB for the DC and RC scenarios are given as

$$P_L(d) = 51.9 + 31.6 \log 10(d) \tag{11}$$

and

$$P_L(d) = 11.2 + 37.6 \log 10(d), \tag{12}$$

where d is the distance between the BS and the train.

Fig. 10 illustrates the measured PL results and the PL models in the DC and RC scenarios. It can be seen that the PL in the DC scenario is approximately 20-30 dB higher than that in the RC scenario. This value corresponds to the penetration loss from the train body. On the other hand, the resulting PL exponents for the DC and MRC cases are 3.16 and 3.76, respectively, which are all much higher than that of 2.0 in the free space model. For the DC it is understandable that the outdoor to indoor propagation condition intensifies the attenuation of the signal power, however, for the RC the main reason which has been explained in [2] [4] is that the train carriage roof would act as a ground plane and thus affect the antenna radiation pattern by causing a null in a certain incidence angle area of the radiation pattern.

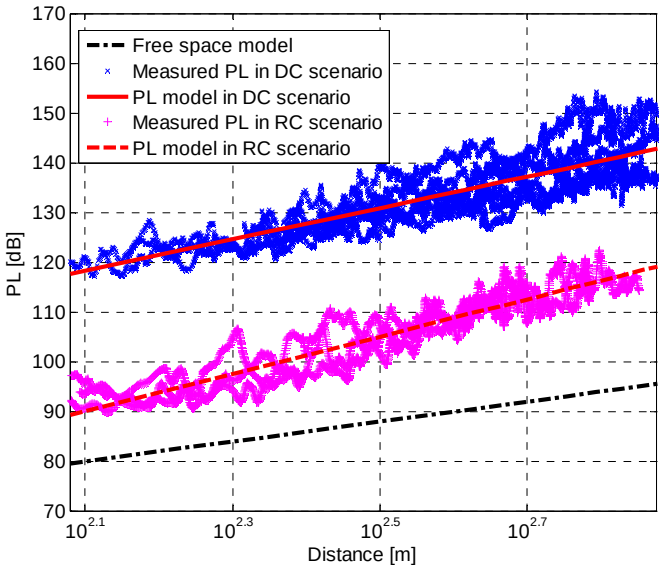

Fig. 10 PLs in the DC and RC scenarios

B. Ricean K-factor

Ricean K-factor is a parameter indicating the temporal fading severity of the radio channel, which can be extracted by the CIRs of removing the large-scale effect. The narrowband K-factor [20] is estimated in the same set of 10 m windows using the classical moment based method in [21], as a function of distance. Fig. 11 presents the cumulative distribution functions (CDFs) of the K-factors and the fitting of the CDFs with a normal distribution in the DC and RC scenarios. A K-factor with a mean of 4.27 dB and a standard deviation of 2.87 dB is observed for the DC case, whereas they are 7.47 dB and 4.39 dB for the RC case. The strength of K-factor in the DC scenario is weaker than that in the RC scenario since the receive antenna placed inside the train carriage encounters more multipath echoes. In addition, the K-factor result for the RC scenario matches the K-factor model with 7 dB mean value and 4 dB standard deviation for the RMa scenario in ITU-R M.2135 model [22].

In Fig. 12, the K-factors are plotted as a function of the distance. The measured K-factors appear a linear downward trend with the increase of distance. To characterize the variation of the K-factor, the linear distance-dependent K-factor models for the DC and RC cases are given as

$$K\left(d\right) = -0.0076d + 7.64 \tag{13}$$

and

$$K\left(d\right) = -0.024d + 15.71. \tag{14}$$

It is noted that the K-factor value in [4] is much larger than that in the RC scenario. One reason is that the K-factor model in [4] refers to the wideband K-factor derived from the data of the main path or the strongest path, and the scattering components in other multipath are not included in the wideband K-factor estimation.

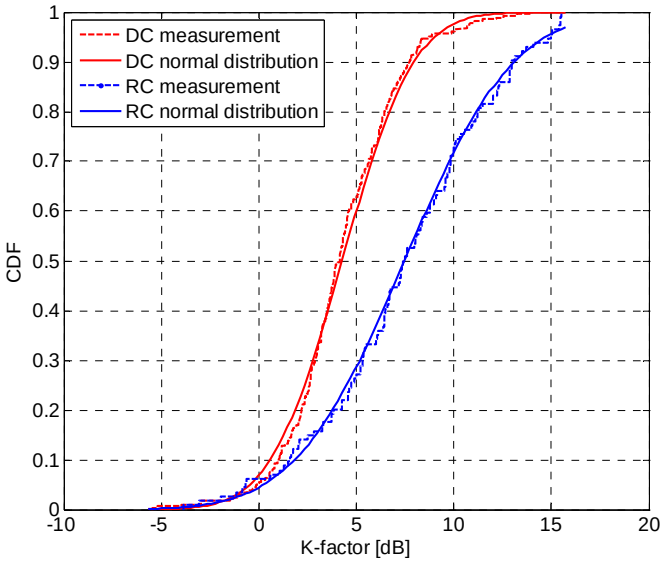

Fig. 11 CDFs of the K-factors in the DC and RC scenarios

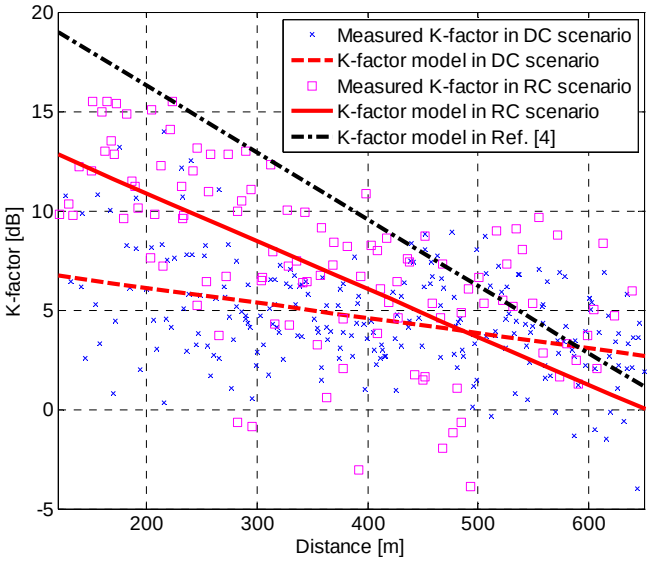

Fig. 12 K-factors as a function of the distance in the DC and RC scenarios

C. RMS Delay Spread

The RMS DS is determined by the PDP at local area, which can be calculated as the standard deviation of the excess time delay weighted with the power [23]. Fig. 13 shows the CDFs of the RMS DSs and the fitting of the CDFs with a lognormal distribution in the DC and RC scenarios. It is obvious that the DC case has the higher RMS DS than the RC case since the indoor antenna receives more multipath waves. The fitting parameters $\mu(\log10(s))$ and $\sigma(\log10(s))$ of the RMS DS for the RC case are -7.68 and 0.57, whereas

those for the DC case are -7.06 and 0.34. It can be found that the RC result is close to the ITU-R M.2135 model [22] in the RMa scenario with the mean value of -7.49 and the standard deviation of 0.55.

Fig. 14 depicts the RMS DSs against the distance. It shows that the RMS DS experience a rising trend with the increase of distance. This is because when the train is moving away BS, increasing multipath waves are likely to be distinguished. The similar phenomenon is also observed in [24] where the RMS DS is modeled as a simple linear function of the distance. Assume that the RMS DS is 0 ns at 0 m, the fitting models for the DC and RC cases are given as

$$\tau_{\mathrm{rms}}\left(d\right)=0.22d \tag{15}$$

and

$$\tau_{\mathrm{rms}}\left(d\right)=0.13d. \tag{16}$$

It can be seen that the cutting scenario in [24] has the larger RMS DS than the measured viaduct scenario no matter whether the antenna is placed inside the carriage or on top of the train.

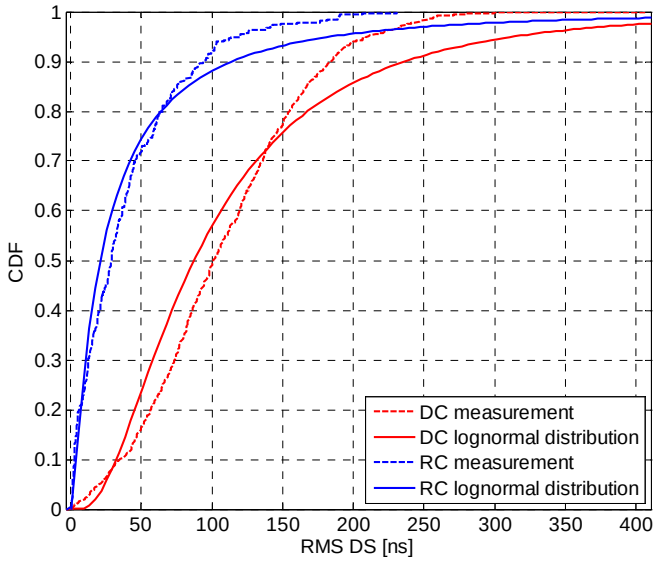

Fig. 13 CDFs of the RMS DSs in the DC and RC scenarios

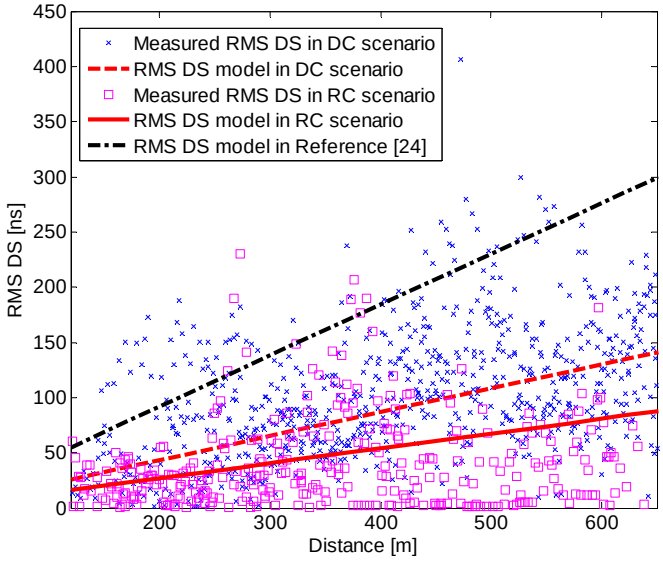

Fig. 14 RMS DSs as a function of the distance in the DC and RC scenarios

D. Spatial Correlation

To investigate the MIMO performance, we focus on the SC between the different antenna elements at both ends of the individual link, namely, single-link SC. Besides, we also consider the multi-link SC [25] which exists due to the environment similarity arising from common scatterers contributing to different links and can significantly affect the performance of coordinated multipoint transmission (CoMP) technology. Based on the measurement data in the single-link region, the single-link SC between two sub-channels, H_{11}^{S} and $H_{22,}^{S}$ is derived. Similarly, according to the effective measurement data in the multi-link region, the multi-link SC between $H_{11}^{M,1}$ and $H_{11}^{M,2}$ is estimated. Fig. 9 illustrates the single-link SC result in the RC scenario and multi-link SC results in the DC and RC scenarios. It is observed that almost 65% of single-link SC values are less than 0.8. For the multi-link SC, the results are optimistic in both DC and RC scenarios where the majority of the correlation coefficients are below 0.8. Moreover, since rich scatterers in the in-train environment lead to a low degree of environment similarity, the DC case has the lower multi-link SC than the RC case. From these results, we can infer that in the plain viaduct scenario the MIMO performance can be improved by means of the cross-polarized antenna configuration at the BS side and the large antenna spacing at the train side. Moreover, CoMP technology could have a good performance in terms of micro-diversity due to the low multi-link SC.

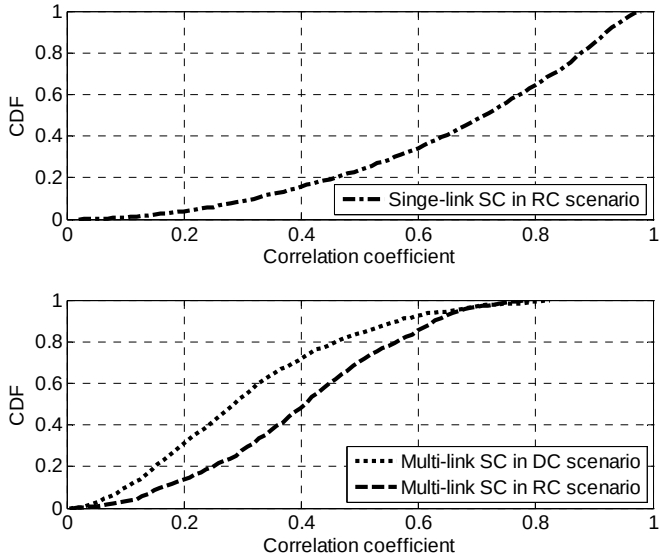

Fig. 9. CDFs of the SCs in the DC and RC scenarios

V. Conclusion

In this paper, the principle and implementation of the LTE-based HSR channel measurement method were presented. The CIR extraction using the CRS is described, and the impacts of CFO and TO on the CIR performance were analyzed, which show that the CFO causes the increase of NF and the fractional TO leads to the power leakage of the CIR. Based on the established system, field measurements taking both DC and RC schemes into account were performed on BT HSR in China. Measurement data were collected and partitioned for the single-link and multi-link channel characterizations. The measurement results proved the feasibility of the proposed method and provided some realistic HSR channel information in the plain viaduct environment. At first, the PL exponents in both the DC and RC scenarios have much higher value than that in the free space propagation scenario. In addition, there are stronger K-factor and smaller RMS DS for the RC case than for the DC case. Finally, 65% of single-link SC values are less than 0.8 under the condition of ±45° cross-polarized antenna configuration at the BS side and 7.6 wavelengths antenna spacing at the train side, and the multi-link SC is found to be relatively low.

Acknowledgement

The authors would like to thank Huisheng Wang and Yuzheng Zhang from China Academy of Railway Sciences for their help to perform the channel measurements, and Long Sun from Huawei for the useful

discussion of LTE railway network structure and configuration. The research was supported in part by the NSFC project under grant No. 61371070, No. 61471030, and Beijing Natural Science Foundation (4142041).

Reference

[1] B. Ai, X. Cheng, T. Kürner, Z. D. Zhong, K. Guan, R. S. He, L. Xiong, D. W. Matolak, D. G. Michelson, and C. B. Rodriguez, “Challenges toward wireless communications for high-speed railway,” *IEEE Tran. Intell. Transp.*, vol. 15, no. 5, pp. 2143-2158, Oct. 2014.

[2] P. Kyösti, “WINNER II channel models part II radio channel measurement and analysis results,” 2007.

[3] R. Parviainen, P. Kyösti, and Y. Hsieh, “Results of high speed train channel measurements,” European Cooperation in the Field of Scientific and Technical Research, Tech. Rep., 2008.

[4] L. Liu, C. Tao, J. H. Qiu, H. J. Chen, L. Yu, W. H. Dong, and Y. Yuan, “Position-based modeling for wireless channel on high-speed railway under a viaduct at 2.35 GHz,” *IEEE J. Sel. Areas Commun.*, vol. 30, no. 4, pp. 834-845, May 2012.

[5] J. Kivinen, T. O. Korhonen, P. Aikio, R. Gruber, P. Vainikainen, and S. G. Haggman, “Wideband radio channel measurement system at 2 GHz,” *IEEE Trans. Instrum. Meas.*, vol. 48, no. 1, pp. 39-44, Feb. 1999.

[6] S. Salous, P. Filippidis, R. Lewenz, I. Hawkins, N. Razavi-Ghods, and M. Abdallah, “Parallel receiver channel sounder for spatial and MIMO characterisation of the mobile radio channel,” *IEE Proc. on Commun.*, vol. 152, no. 6, pp. 912-918, Dec. 2005.

[7] L. Liu, C. Tao, T. Zhou, Y. P. Zhao, X. F. Yin, and H. J. Chen, “A highly efficient channel sounding method based on cellular communications for high-speed railway scenarios,” *EURASIP J. Wireless. Commun.*, vol. 2012, Oct. 2012. doi:10.1186/1687-1499-2012-307

[8] R. S. He, Z. D. Zhong, B. Ai, and J. Ding, “An empirical path loss model and fading analysis for high-speed railway viaduct scenarios,” *IEEE Antennas Wireless Propag. Lett.*, vol. 10, pp. 808-812, Aug. 2011.

[9] J. H. Qiu, C. Tao, L. Liu, and Z. H. Tan, “Broadband channel measurement for the high-speed railway based on WCDMA,” in *Proc. IEEE 75th VTC-Spring*, Yokohama, Japan, May 2012, pp.1-5.

[10] [Online]. Available: http://www.huawei.com/za/static/HW-371906.pdf

[11] S. Salous, Radio Propagation Measurement and Channel Modelling, John Wiley and Sons Ltd., Wiley,

2013.

[12] 3GPP TS 36.211 V9.1.0, Technical Specification Group Radio Access Network; Evolved Universal Terrestrial Radio Access (E-UTRA); Physical Channels and Modulation, 2010.

[13] [Online]. Available: http://www.channelsounder.de/csprinciple_site2.html

[14] T. Pedersen, G. Steinböck, and B. Fleury, “Modeling of reverberant radio channels using propagation graphs,” *IEEE Trans. Antennas Propag.*, vol. 60, no. 12, pp. 5978-5988, Dec. 2012.

[15] [Online]. Available: http://yctnt.en.b2b168.com/shop/supply/13000206.html

[16] [Online]. Available: http://www.biwin.com.cn/en/prodetail.asp?bid=22&sid=108&id=0&pid=37

[17] [Online]. Available: http://www.cucgx.com/en-productview.aspx?infoid=1016

[18] Sencity Rail Antenna: 1399.17.0039 HUBER+SUHNER data sheet, HUBER+SUHNERAG RF Industrial, 2010.

[19] X. Zhao, J. Kivinen, P. Vainikainen, and K. Skog, “Propagation characteristics for wideband outdoor mobile communications at 5.3 GHz,” *IEEE J. Sel. Areas Commun.*, vol. 20, no. 3, pp. 507-514, Apr. 2002.

[20] T. Zhou, C. Tao, L. Liu, and Z. H. Tan, “Ricean K-factor measurements and analysis for wideband high-speed railway channels at 2.35 GHz,” *Radioengineering*, vol. 23, no. 2, pp. 578-585, Jun. 2014.

[21] L. Greenstein, D. Michelson, and V. Erceg, “Moment-method estimation of the Ricean K-factor,” *IEEE Comm. Lett.*, vol. 3, no. 6, pp. 175-176, 1999.

[22] ITU-R M.2135, Guidelines for evaluation of radio interface technologies for IMT-Advanced, 2009.

[23] J. H. Zhang, D. Dong, Y. P. Liang, X. Nie, X. Y. Gao, Y. Zhang, C. Huang, and G. Y. Liu, “Propagation characteristics of wideband MIMO channel in urban micro- and macrocells,” in *Proc. IEEE 19th PIMRC*, Cannes, France, Sept. 2008, pp. 1-6.

[24] L. Tian, J. H. Zhang, C. Pan, L. Liu, and C. Tao, “Small scale fading characteristics of wideband radio channel in the U-shape cutting of high-speed railway,” in *Proc. IEEE 78th VTC-Fall*, Las Vegas, USA, Sept. 2013, pp.1-6.

[25] X. Cheng, C.-X. Wang, H. Wang, X. Gao, X.-H. You, D. Yuan, B. Ai, Q. Huo, L. Song, and B. Jiao, “Cooperative MIMO channel modeling and multi-link spatial correlation properties,” *IEEE J. Sel. Areas Commun.*, vol. 30, no. 2, Feb. 2012, pp. 388-396.